Materials Horizons

ROYAL SOCIETY OF CHEMISTRY

COMMUNICATION

View Article Online
View Journal | View Issue

Cite this: *Mater. Horiz.*, 2025, 12, 6765

Received 18th April 2025,
Accepted 9th June 2025

DOI: 10.1039/d5mh00738k

rsc.li/materials-horizons

Boosting thermal conductivity of boron nitride incorporated polymer composites *via* hydrogen bonding engineering†

Wenbo Lin,[acd] Yanfeng Li,[b] Xirui Liu,[ac] Rui Xu,[ac] Jiajing Huang,[acd] Zhiyuan Jiang,[e] Zhiguo Qu,[f] Kai Xi *[b] and Yue Lin *[acd]

Enhancing the thermal conductivity of polymer-based composites is critical for effective thermal management in power electronics. A common strategy involves incorporating high-thermal-conductivity fillers such as graphene and boron nitride nanosheets (BNNS). However, practical enhancements often fall short of theoretical predictions due to interfacial thermal resistance ($R_{Kapitza}$). Here, we address this challenge by engineering the hydrogen bond density (HBD) at the filler–matrix interface. By grafting 3,4-dihydroxyphenylalanine (DOPA) onto polyvinyl alcohol (PVA), we synthesized PVA-D*X* matrices (*X* = 0, 8, 12, 17, 24) with tunable HBDs. Incorporation of BNNS into these matrices revealed that higher interfacial HBD significantly reduces $R_{Kapitza}$, thereby enhancing the composite's thermal conductivity (κ_c). We achieved an exceptionally low $R_{Kapitza}$ of 0.60 × 10^{-8} m^2 K W^{-1}, corresponding to a filler effectiveness ($\kappa_c/\varnothing_f$) of 120 W m^{-1} K^{-1}. Notably, at a BNNS loading of 70 vol%, increasing the interfacial HBD to 2.14 mmol cm^{-3} achieves a κ_c of 51.01 W m^{-1} K^{-1}, which is 1.45 times higher than the 35.29 W m^{-1} K^{-1} attained at an HBD of 0.5 mmol cm^{-3}. This study underscores the critical role of interfacial hydrogen bonding in optimizing thermal transport and provides a robust framework for designing high-performance polymer composites for advanced thermal management applications.

New concepts

Achieving high thermal conductivity in polymer composites is fundamentally limited by interfacial Kapitza resistance ($R_{Kapitza}$). Covalent grafting, π–π stacking, and other interfacial chemistries are well studied at the nanometer level, yet their impact has scarcely been demonstrated in centimetre scale, bulk materials where heat must traverse billions of filler–matrix contacts. We introduce hydrogen bond density (HBD) engineering as a scalably tunable, metrical handle that translates molecular chemistry into macroscopic heat transport. By grafting 3,4-dihydroxyphenylalanine onto poly(vinyl alcohol) we raise the interfacial HBD from 0.50 to 2.14 mmol cm^{-3} without altering filler morphology. This single parameter jump cuts $R_{Kapitza}$ to 0.60 × 10^{-8} m^2 K W^{-1} and boosts bulk thermal conductivity from 35.3 to 51.0 W m^{-1} K^{-1} at 70 vol% boron nitride nanosheets. Correlated experiments and molecular dynamics expose a near linear HBD–$R_{Kapitza}$ relation that plateaus beyond a critical density, revealing a previously unrecognised upper bound for non-covalent heat transfer. Our work recasts interfacial optimisation from empirical filler alignment to quantifiable chemistry control, offering a transferable design rule for high power electronics, soft robotics, and next generation encapsulants where centimetre scale thermal highways are demanded.

Introduction

Polymer-based composites are extensively used in thermal management for power electronics due to their cost-efficiency, ease of processing, and flexibility, offering a distinct advantage over metal- and ceramic-based materials.[1–3] A widely employed strategy to improve the thermal conductivity of these composites involves incorporating high-thermal-conductivity fillers, such as metals,[4–7] ceramics,[8–10] graphene,[11–14] and liquid metals.[15–17] According to effective medium theory,[18–20] adding fillers with inherently higher thermal conductivity is expected to significantly enhance the overall thermal performance of the composite.

[a] *State Key Laboratory of Functional Crystals and Devices, State Key Laboratory of Structural Chemistry, and Fujian Key Laboratory of Nanomaterials, Fujian Institute of Research on the Structure of Matter, Chinese Academy of Sciences, Fuzhou, Fujian, 350002, P. R. China. E-mail: linyue@fjirsm.ac.cn*
[b] *School of Chemistry, Engineering Research Center of Energy Storage Materials and Devices, Ministry of Education, National Innovation Platform (Center) for Industry-Education Integration of Energy Storage Technology, State Key Laboratory for Electrical Insulation and Power Equipment, Engineering Research Center of Energy Storage Material and Chemistry, Universities of Shaanxi Province, Xi'an Jiaotong University, Xi'an 710049, China. E-mail: kx210.cam@xjtu.edu.cn*
[c] *Fujian College, University of Chinese Academy of Sciences, Fujian, Fuzhou 350007, P. R. China*
[d] *University of Chinese Academy of Sciences, Beijing, 100049, P. R. China*
[e] *School of Chemical Engineering and Technology, Xi'an Jiaotong University, No. 28 Xianning west road, Xi'an, Shaanxi 710049, P. R. China*
[f] *MOE Key Laboratory of Thermo-Fluid Science and Engineering, School of Energy and Power Engineering, Xi'an Jiaotong University, Xi'an, Shaanxi 710049, China*
† Electronic supplementary information (ESI) available. See DOI: https://doi.org/10.1039/d5mh00738k

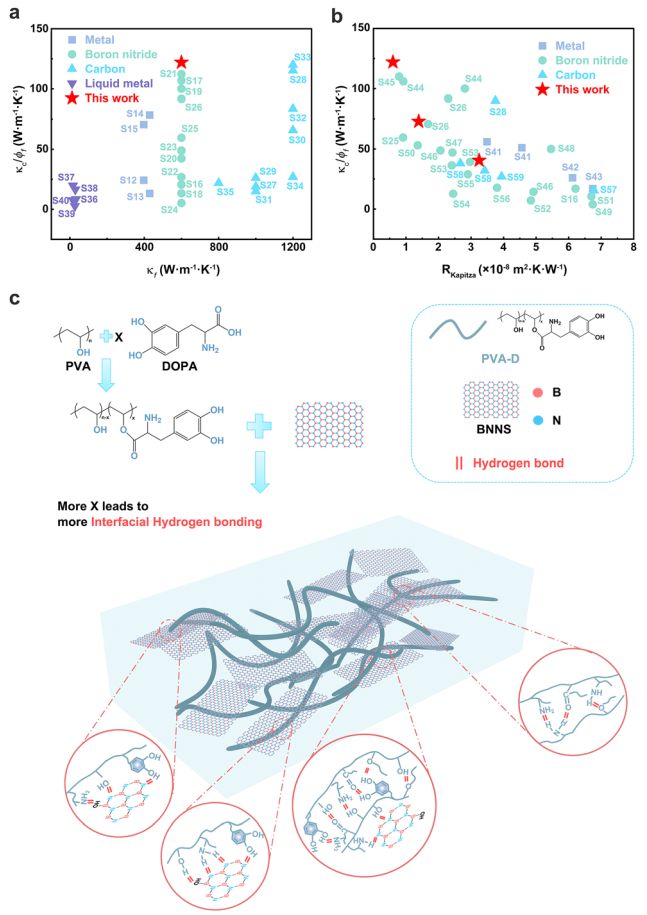

Fig. 1 Fabrication of BN/PVA-D*X* films *via* hydrogen bond engineering. (a) Comparison of filler-effectiveness in volumetric thermal conductivity, defined as the composite thermal conductivity κ_c per unit filler volume $\varnothing_f$ for fillers with different thermal conductivities κ_f. Detailed data are provided in Table S36 in ESI.† (b) Variation of $\kappa_c/\varnothing_f$ under different interfacial thermal resistance $R_{Kapitza}$. Detailed data are given in Table S37 in ESI.† (c) Schematic illustration of the fabrication process for BN/PVA-D*X* films, highlighting the role of hydrogen-bond engineering.

However, contrary to theoretical predictions, practical outcomes in the literature often reveal that this enhancement is not as effective as anticipated (Fig. 1(a)). Specifically, the effectiveness of fillers, measured as the thermal conductivity of the composite (κ_c) per unit volume of filler ($\varnothing_f$), varies widely. For instance, despite the high thermal conductivity of boron nitride (BN) fillers ($\sim$600 W m^{-1} K^{-1}),[21] their effectiveness in polymer matrixed composites fluctuates by an order of magnitude, from 20 W m^{-1} K^{-1} per unit volume to 120 W m^{-1} K^{-1} per unit volume. A similar trend is observed for graphene-polymer composites, where the exceptional thermal conductivity of graphene ($\sim$1200 W m^{-1} K^{-1})[22] does not proportionally translate into the composite material. These observations suggest that the intrinsic thermal conductivity of the fillers is not the sole or dominant factor governing the overall thermal performance of the composites.

This discrepancy raises a critical question: apart from the filler's intrinsic thermal conductivity (κ_f), what factors primarily influence the κ_c Addressing this issue is essential, as filler content influences not only thermal performance but also impacts other key properties such as mechanical strength, electrical conductivity, and optical characteristics.[23–26] While increasing the filler content typically enhances κ_c, it might also adversely affect mechanical properties,[27] limiting the composite's applicability in practical settings. Thus, it becomes crucial to optimize filler efficiency—ensuring the filler maximizes its contribution to κ_c while minimizing detrimental effects on other properties. This balance is key to design high-performance polymer composites tailored for applications like advanced thermal management.

Our analysis of literature data reveals that interfacial thermal resistance ($R_{Kapitza}$), also known as Kapitza resistance, plays a pivotal role in limiting the thermal performance of composites.[28–30] Regardless of the filler type, the effectiveness of fillers in enhancing κ_c improves significantly when the $R_{Kapitza}$ drops below 3×10^{-8} m^2 K W^{-1} (Fig. 1(b)). This $R_{Kapitza}$, characterized by a temperature discontinuity at material boundaries,[31,32] acts as a significant bottleneck in heat transfer across interfaces. For example, even though BN fillers possess high intrinsic thermal conductivity, BN-polymer composites typically achieve below 20 W m^{-1} K^{-1} (Fig. S1, ESI†), primarily due to high $R_{Kapitza}$.[33–35] Consequently, minimizing $R_{Kapitza}$ is essential for enhancing the thermal performance of polymer composites.

Various strategies have been employed to enhance the κ_c of polymer-based composites, including surface modifications, improving filler aspect ratios, and constructing continuous pathways through techniques such as filler alignment.[36–39] While these approaches have successfully demonstrated improvements in κ_c, the underlying mechanism—specifically, the reduction of $R_{Kapitza}$—has only been qualitatively discussed in some studies. For instance, Huang *et al.*[40] showed that surface modifiers chemically similar to the fillers are more effective in reducing $R_{Kapitza}$. Yan *et al.*[41] demonstrated that increasing the aspect ratio of BN nanosheets (BNNS) reduces the number of interfaces, thereby lowering $R_{Kapitza}$. Similarly, Gao *et al.*[42] significantly improved κ_c (12.13 W m^{-1} K^{-1}) by fabricating a BN-based composite with a neuron-like network structure to reduce the number of interfaces. Despite these advancements, a comprehensive understanding of the factors controlling $R_{Kapitza}$ and strategies to manipulate it remain elusive. Moreover, few studies have delved into the detailed interactions between fillers and matrices, as well as their impact on thermal performance. Understanding how these interactions influence thermal transport is crucial for optimizing composite designs for more effective heat dissipation.

In this study, we demonstrate that engineering non-covalent interaction, specially, hydrogen bonding, is an effective way to enhance the κ_c of BN-polymer composites. By adjusting the molar ratio of polyvinyl alcohol (PVA) to 3,4-dihydroxyphenylalanine (DOPA) in the polymer matrix, we control the hydrogen bond density (HBD), which in turn affects the $R_{Kapitza}$ and κ_c. By blending BNNS fillers with matrices of varying densities of hydrogen bond capable groups, we successfully manipulate the κ_c through hydrogen bonding engineering (Fig. 1c).

Remarkably, in a PVA-D matrix with a high HBD of 4.04 mmol cm^{-3}, the composite achieved a κ_c of 51.01 W m^{-1} K^{-1} at a $\varnothing_f$ of 0.7 (70 vol%). This high efficiency is attributed to the markedly low $R_{Kapitza}$ (with lowest value of 0.60×10^{-8} m^2 K W^{-1}) achieved by strong interfacial hydrogen bonding. Overall, this study highlights the potential of hydrogen bond modulation as an effective strategy for enhancing both interfacial and bulk κ_c in polymer-based composites. These insights offer valuable guidance for the development of advanced composites with superior thermal management capabilities.

Experimental section

Materials

Hexagonal boron nitride (h-BN) powders with average particle size of 30 μm were purchased from Dandong Rijin Science and Technology Co., Ltd (China). PVA ($M_w \sim 205\,000$) powders were provided by Shanghai Macklin Biochemical Technology Co., Ltd (Shanghai, China), 3,4-dihydroxyphenylalanine (DOPA, 99%) and sodium hydrogen sulfate monohydrate ($NaHSO_4 \cdot H_2O$,99%) was obtained from Adamas Reagent Co., Ltd (Shanghai, China), dimethyl sulfoxide (DMSO) was purchased from Sinopharm Chemical Reagent Co., Ltd (Shanghai, China), All chemicals were used without further purification.

Exfoliation of h-BN

Deionized water (50 g) and ethanol (50 g) were mixed with 1 : 1 weight ratio, and then 1.13 g of h-BN powder were added to the mixed solution. The solution was subjected to bath ultrasonication at 40 kHz and 600 W nominal power for 30 min. The bath temperature was maintained below 30 °C by intermittent cooling to avoid re-aggregation or oxidation. This protocol consistently yields BN nanosheets with an average aspect ratio of ~314, as determined by AFM and SEM analyses. High-pressure homogenization was carried out by microfluidizer (PSI-20, Alpharmaca Biotechnology Co., China) at various pressures (50, 100, 150, and 180 Mpa) for 100 cycles, and at 180 Mpa for different cycles (20, 50 and 100 cycles) to exfoliation h-BN. This process yielded boron nitride nanosheets.

Synthesis of PVA-D*X* (*X* = 8, 12, 17, 24)

PVA (1.76 g, 40 mmol) was dissolved in DMSO (30 ml). After dissolution, 0.75 g of $NaHSO_4 \cdot H_2O$ was added. The temperature was then reduced to 80 °C, and different amounts of DOPA (10–40 mmol) were added. The reaction was then kept at 80 °C under N_2 for 24 hours. Then, the solution was purified by dialysis for 72 hours using a dialysis membrane (MWCO 3500 Da, Viskase, America). The resulting PVA-D powders were obtained through freeze-drying. These polymers were designated as PVA-D*X* (*X* = 8, 12, 17, 24), where PVA-D0 represented pure PVA. The theoretical PVA : DOPA molar ratios were 100 : 25, 100 : 50, 100 : 75, and 100 : 100, while the actual ratios were 100 : 8, 100 : 12, 100 : 17, and 100 : 24.

Composite film fabrication

The PVA-D powders were dissolved in deionized water to obtain a PVA-D aqueous solution (10 g L^{-1}). The PVA-D solution was mixed with the BNNS dispersion (10 g L^{-1}, obtained by exfoliating h-BN at 180 MPa for 50 cycles, with aspect ratio of 314) under magnetic stirring. The bath ultrasonication was then applied for 30 min to obtain homogeneous dispersion. Because of the strong hydrogen-bonding affinity between PVA-D*X* and BNNS, the nanosheets remain uniformly dispersed in the PVA-D*X* aqueous solution for at least 10 h, with no visible sedimentation, which is clear evidence of excellent dispersion stability. The pH of the solution was then adjusted to be acidic (pH = 3), After that, the mixture was stirred at 1000 rpm for 12 hours by magnetic stirrer. The obtained suspension was vacuum filtered through a Polycarbonate membrane with a pore size of 0.08 μm. The BN/PVA-D paper could be directly peeled off from the membrane. Then, it dried under vacuum at 80 °C for 12 hours. Finally, The BNNS films were obtained by employing hot pressing method, this involved applying a pressure of 25–28 MPa for 40 minutes each at three different temperatures: 50 °C, 80 °C, and 100 °C.

Characterization

The morphology and microstructure of BNNS and BN/PVA-D*X* composite films were examined by scanning electron microscopy (15 kV, EM-30+, Coxem, Korea). The morphology of BNNS were examined by an atomic force microscope (AFM, Dimension ICON, Bruker, Germany). The structures of bulk h-BN and BNNS were investigated using X-ray diffraction (XRD, MiniFlex 600, Rigaku, Japan), while the structures of bulk h-BN, BNNS, PVA-D*X*, and BN/PVA-D*X* were analyzed using Fourier transform infrared spectroscopy (FTIR, VERTEX70, Bruker, Germany). The synthesis of the PVA-D*X* polymers was explored by means of Ultraviolet-visible (UV-vis) spectrophotometer (Lambda950, PerkinElmer, USA). The equation for calculating the thermal conductivity was $\kappa_c = \alpha \times C_p \times \rho$, where α, C_p, and ρ are the thermal diffusivity, specific heat capacity, and the density of the sample, respectively. The thermal diffusivity of the composite films was measured by laser flash method (Discovery Xenon Flash 200+, TA instrument, USA), the thermal capacity was obtained by differential scanning calorimetry (DSC 250, TA instrument, USA), and the density was calculated by the equation:

$$\rho = \frac{m}{v}$$

The mass fraction of BN (φ) is calculated using specific heat capacities, according to the formula:

$$\varphi = \frac{C_{composite} - C_{polymer}}{C_{BN} - C_{polymer}},$$

where $C_{composite}$ represents the specific heat capacity of the composite material (Tables S34 and S35, ESI†), C_{BN} (0.79 J g^{-1} K^{-1})[9] and $C_{polymer}$ (Table S33, ESI†) are the specific heat capacities of BN and the polymer, respectively. Subsequently, the BN volume fraction ($\varnothing_f$) is determined from the

mass fraction using the following formula:

$$\varnothing_f = \frac{\varphi/\rho_{BN}}{\varphi/\rho_{BN} + (1-\varphi)/\rho_{polymer}},$$

where ρ_{BN} is 2.2 g cm^{-3}, and $\rho_{polymer}$ is 1.3 g cm^{-3}.

Results and discussion

Synthesis of PVA-D*X* with engineered hydrogen bond density

To precisely manipulate the HBD within the composite material, we engineered the polymer matrix by bonding capabilities, ease of modification, and compatibility with various incorporating DOPA, a molecule rich in hydrogen bond capable groups, into PVA backbone. PVA was selected due to its inherent hydrogen additives. By introducing calculated amounts of DOPA, we added additional functional groups capable of hydrogen bonding into the matrix.

We synthesized PVA-D*X* through an esterification reaction between the carboxyl groups (–COOH) of DOPA and the hydroxyl groups (–OH) of PVA, forming stable ester bonds (–COO–). Sodium bisulfate monohydrate ($NaHSO_4{\cdot}H_2O$) served as a catalyst by absorbing the water produced during the reaction and providing a mild acidic environment through the release of H^+ ions.[43,44] This process resulted in a polymer matrix with increased hydrogen bond capable groups, thereby strengthening the hydrogen bonding network within the material. To create matrices with varying HBDs, we prepared a series of PVA-D polymers with different degrees of DOPA grafting, denoted as PVA-D*X*. We defined *X* as the number of vinyl alcohol (VA) units, out of every 100 VA units in PVA, that are chemically reacted with DOPA units. Notably, $X = 0$ corresponds to pure PVA with no DOPA substitution. In the synthesis, we fixed the molar amount of PVA at 40 mmol (1.76 g) and varied the amount of DOPA added (10–40 mmol, 1.97–7.88 g), corresponding to PVA-to-DOPA molar ratios of 4 : 1, 4 : 2, 4 : 3, and 4 : 4. After the reaction, excess DOPA was subsequently removed by dialysis to ensure purity. As shown in Fig. 2(a), the PVA-D samples exhibited a distinct absorption peak at 280 nm—absent in pure PVA, indicating successful grafting of DOPA onto the PVA backbone. The intensity of this absorption peak increased proportionally with the initial DOPA content, confirming that a higher DOPA input resulted in greater incorporation into the polymer matrix. Through ultraviolet-visible (UV-vis) absorbance measurements at 280 nm (the characteristic catechol absorption peak),[45] we quantified the DOPA content and thereby the degree of substitution (*X*), which ranged from $X = 8$ to $X = 24$ (details provided in the ESI,† Session S1). A summary of these values is provided in Table S1 (ESI†).

Fourier-transform infrared (FTIR) spectroscopy also validated the successful grafting of DOPA (Fig. 2(b), details provided in the ESI,† Session S3). New absorption peaks appeared at 1730 cm^{-1}, corresponding to the carbonyl (C═O) stretching vibration of the –COO–, and at 1050 cm^{-1}, attributed to the C–O–C stretching vibration, confirming the formation of ester linkages.[46,47] Additionally, the incorporation of DOPA introduced amino ($–NH_2$), –C═O, and –C–O–C– groups into the polymer, contributing to the hydrogen bonding network. The overlapping of –OH and –NH stretching vibrations resulted in an expanded absorption band in the region of 2980 to 3640 cm^{-1}.

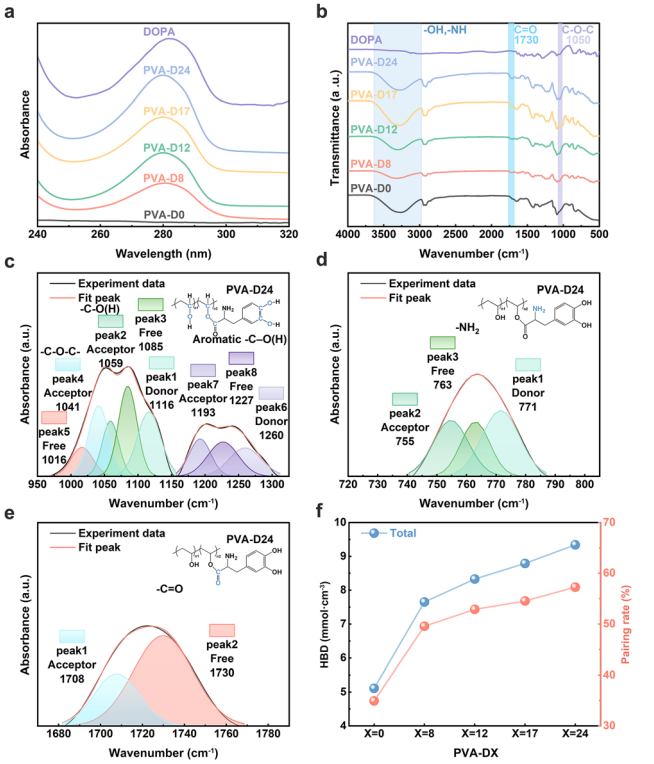

Fig. 2 Characterization, and hydrogen bonding analysis of PVA-D*X* matrices. (a) Ultraviolet-visible (UV-vis) absorbance spectra of different PVA-D. (b) Fourier-transform infrared (FTIR) spectra of various PVA-D. ATR-FTIR deconvolution of (c) the –C–O(H) region, (d) the $–NH_2$ region, and (e) the –C═O region in PVA-D24. (f) The hydrogen bond density (HBD) in different PVA-D*X* matrices.

To quantify the HBD within the matrices, we performed FTIR spectral deconvolution (Fig. 2(c)–(e), details provided in the ESI,† Session S4). Distinct wavenumber shifts in the IR spectra allowed us to identify how various functional groups transition between hydrogen bond donor and acceptor states. For example, in Fig. 2(c), the C–O(H) peak of VA units (initially at 1085 cm^{-1}) and that of VA-DOPA units (initially at 1227 cm^{-1}) shift to higher wavenumbers (1116 cm^{-1} and 1260 cm^{-1}, respectively) when the –OH group acts as a hydrogen bond donor, and to lower wavenumbers (1059 cm^{-1} and 1193 cm^{-1}) when it serves as an acceptor.[48] Similarly, the $–NH_2$ peak (free: 763 cm^{-1}) shifts down to 755 cm^{-1} as an acceptor and up to 771 cm^{-1} as a donor[49] (Fig. 2(d)). Groups that function solely as acceptors follow consistent trends: the –C═O peak (free: 1730 cm^{-1}) moves to a lower wavenumber (1708 cm^{-1}) upon forming hydrogen bonding,[50] while the –C–O–C– peak (free: 1016 cm^{-1}) shifts to a higher wavenumber (1041 cm^{-1}) when acting as an acceptor[51] (Fig. 2(c) and (e)).

By deconvoluting these spectral features, we determined the total HBD ($N^{HB}_{PVA\text{-}DX}$) formed by –OH, $–NH_2$, –C═O, and –C–O–C– groups in each PVA-D sample. Although the total pool of hydrogen bonding capable groups increased only modestly with

DOPA substitution (from 29.55 mmol cm^{-3} in PVA-D0 to 32.89 mmol cm^{-3} in PVA-D24; Table S15, ESI†), the actual number of formed hydrogen bonds rose substantially—by 83%—from 5.11 mmol cm^{-3} to 9.34 mmol cm^{-3} (Fig. 2(f)). This indicates that the proportion of functional groups participating in hydrogen bonding increased significantly with DOPA addition. Correspondingly, the 'pairing rate' (the fraction of functional groups engaged in hydrogen bonding) climbed from 34.91% in PVA-D0 to 49.57% in PVA-D8 and further to 57.26% in PVA-D24.

This pronounced enhancement can be attributed to the multifunctionality of DOPA. Its catechol moieties (featuring *ortho*-dihydroxy groups) and $-NH_2$ groups collectively provide abundant hydrogen bonding sites, enabling more extensive network formation within a limited volume.[52] Moreover, the esterification that grafts DOPA onto PVA introduces additional –C═O groups, which readily act as hydrogen bond acceptors. Together, these newly formed functionalities synergize with the existing –OH and $-NH_2$ groups, facilitating a denser and more robust hydrogen bonding network that becomes increasingly pronounced as the DOPA content rises.

Exfoliation of BNNS fillers and preparation of BN/PVA-D*X* composites

After establishing PVA-D*X* matrices with tunable HBDs, we incorporated BNNS as fillers to fabricate the composites. The B–N bonds within BNNS could form synergistic hydrogen bonds with the PVA-D matrix, potentially enhancing interfacial interactions. To obtain BNNS, we exfoliated hexagonal BN (h-BN) using a high-pressure microfluidization technique (Fig. 3(a)). Under ultra-high pressures of up to 200 MPa, microjets are forced through microchannels at extremely high shear rates, enabling rapid and efficient exfoliation of bulk h-BN into few-layer BNNS[41,53] (details provided in the ESI,† Session S5).

We first explored the influence of pressure on the exfoliation process, conducting 100 consecutive cycles at pressures of 50, 100, 150, and 180 MPa. Atomic force microscopy (AFM, Fig. 3(d) and Fig. S11e–h, ESI†) revealed a clear trend: as the pressure increased, the BNNS thickness decreased (Fig. 3(e)). As observed in scanning electron microscopy (SEM, Fig. 3(b) and Fig. S11a–d, ESI†), lateral dimensions followed a similar trend, decreasing from an average of 1.7 μm at 50 MPa to 1.5 μm at 150 MPa, before unexpectedly increasing to 2.2 μm at 180 MPa (Fig. 3(c)). This increase in lateral size at 180 MPa, combined with the reduced thickness (7.08 nm at 180 MPa *vs.* 9.8 nm at 50 MPa), yielded a higher aspect ratio of ~308, compared to ~200 for BNNS produced at lower pressures (Fig. 3(f)). To further confirm these conditions, we varied the number of cycles at a constant pressure of 180 MPa (20, 50, and 100 cycles) and observed similar high aspect ratios (Fig. 3(g)). We ultimately selected BNNS prepared at 180 MPa and 50 cycles for composite fabrication, achieving an average lateral size of 2.254 μm (Fig. S12a, ESI†), thickness of 7.182 nm (Fig. S12b, ESI†), and an aspect ratio of 314.

Preparation and characterization of BN/PVA-D*X* films with controlled hydrogen bonding densities

After establishing the PVA-D*X* matrices and BNNS as fillers, we fabricated a series of BN/PVA-D*X* composite films with

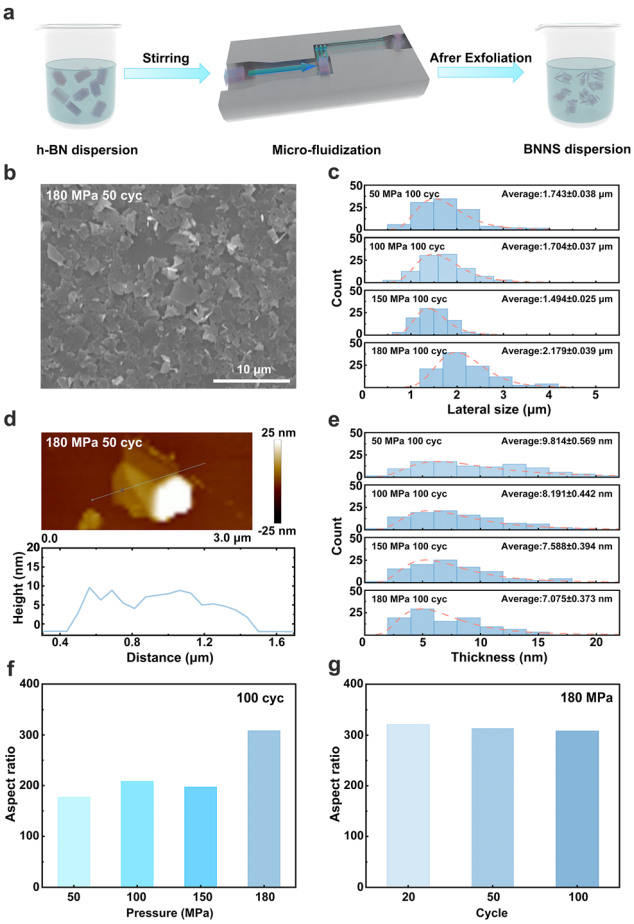

Fig. 3 Characterization of BNNS exfoliated by microfluidization. (a) The microfluidization process utilized for exfoliating BNNS from h-BN. (b) Scanning electron microscopy (SEM) images of BNNS exfoliated under 180 MPa and 50 cycles. (c) Lateral size distribution of BNNS prepared under different applied pressures (50, 100, 150, and 180 MPa) for 100 cycles. (d) Atomic force microscopy (AFM) images of BNNS exfoliated at 180 MPa and 50 cycles, showing flakes with a thickness of approximately 7 nm and corresponding cross-sectional profiles. (e) Thickness distribution of BNNS prepared under different applied pressures (50, 100, 150, and 180 MPa) for 100 cycles. (f) Aspect ratios of BNNS prepared as a function of applied pressure. (g) Aspect ratios of BNNS prepared as a function of applied cycles.

controlled HBDs. The composites were prepared by blending the PVA-D*X* matrices with BNNS, followed by vacuum filtration and hot-pressing (Fig. 4(a)), resulting in films approximately 26 μm thick. Within these composites (Fig. 4(b)), the BNNS sheets are stacked parallel to the film surface, creating a layered, nacre-like microstructure (Fig. 4(c)). Such an arrangement imparts pronounced anisotropy in κ_c, favoring heat flow along the in-plane direction (Fig. S17, ESI†).

To further elucidate how tuning the matrix's hydrogen-bonding functionalities influences the overall HBD in the composites, we performed FTIR spectral deconvolution on key hydrogen bonding donor and acceptor groups: –OH, $-NH_2$, –C–O–C–, –C═O, and B–N (Fig. 4(d)–(h); details provided in the ESI,† Session S4). The observed wavenumber shifts of these functional groups, reflecting donor or acceptor states, closely mirror the trends seen

in the neat PVA-D*X* matrices. Note that, in the presence of BNNS, the –NH_2 wagging and twisting vibrations (740–790 cm^{-1}) overlap with the out-of-plane B–N–B bending modes (690–823 cm^{-1}). As a result, changes in –NH_2 bonding are assessed using its secondary amide N–H bending region (1610–1690 cm^{-1}). Additionally, the newly introduced B–N bonds serve as hydrogen bonding acceptors. For instance, the B–N peak (free: 1334 cm^{-1}) downshifts to 1311 cm^{-1} upon hydrogen bonding (Fig. 4(h)).

Our quantitative analysis reveals a pronounced enhancement in hydrogen bonding. As the DOPA substitution (*X*) increased from 0 to 24, the HBD ($N^{HB}_{BN/PVA\text{-}DX}$) rose by 92%, from 2.10 mmol cm^{-3} to 4.04 mmol cm^{-3} (Fig. 4(i)). By contrast, the total concentration of hydrogen bonding capable groups in PVA-D matrices increased by only 12% (from 8.74 mmol cm^{-3} to 9.78 mmol cm^{-3}; Table S30, ESI†). Notably, the majority of this improvement stems from enhanced matrix–BNNS interfacial hydrogen bonding, which surged by 328% (from 0.50 mmol cm^{-3} to 2.14 mmol cm^{-3}; Fig. 4(i) and Table S29, ESI†). These findings demonstrate that elevating the DOPA content in the matrix effectively strengthens the hydrogen bonding network across the matrix–BNNS interface, thereby significantly increasing the overall HBD in the BN/PVA-D*X* composites.

Thermal properties of BN/PVA-D*X* films featuring engineered hydrogen bond density

To elucidate how interfacial HBD affects thermal transport, we conducted thermal analysis on BN/PVA-D*X* composites containing 70 vol% BNNS (Fig. 5(a)). By systematically increasing the interfacial HBD from 0.50 mmol cm^{-3} (BN/PVA-D0) to 2.14 mmol cm^{-3} (BN/PVA-D24), we observed a 14% rise in heat capacity (C_p)—from 0.970 to 1.105 J g^{-1} K^{-1}. Alongside this increase in C_p, the thermal diffusivity (α) was enhanced by 26% (from 19.6 to 24.7 mm^2 s^{-1}), implying more efficient phonon transport in high-HBD systems. As a result, both the elevated C_p and improved α synergistically boost the in-plane κ_c by 45%—from 35.29 to 51.01 W m^{-1} K^{-1}. Notably, although the interfacial HBD at *X* = 24 is 13% higher than that at *X* = 17, the corresponding κ_c (51.01 *vs.* 50.49 W m^{-1} K^{-1}) differs by only 1%, suggesting a saturation effect at high HBD levels. To probe the mechanism underpinning these observations, we employed Nan's model[54] to calculate the $R_{Kapitza}$ (details provided in the ESI,† Session S7), The results indicate that, $R_{Kapitza}$ decreases from 1.87 × 10^{-8} m^2 K W^{-1} to 1.39 × 10^{-8} m^2 K W^{-1} as the interfacial HBD increases from 0.50 to 2.14 mmol cm^{-3} (Fig. 5(a) bottom). Fig. S15 (ESI†)

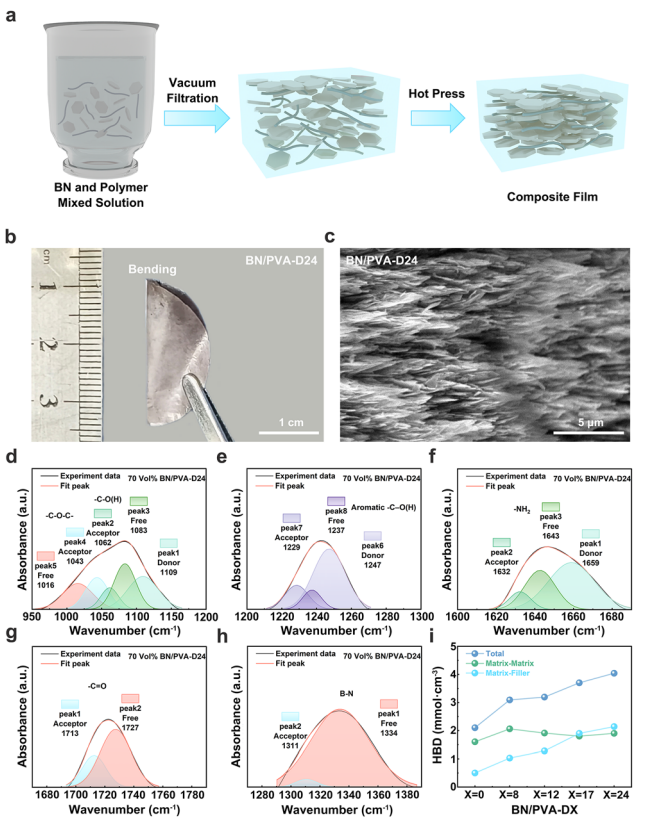

Fig. 4 Fabrication, characterization, and hydrogen bonding analysis of BN/PVA-D*X* composite films. (a) The fabrication process of BN/PVA-D*X* composite films by filtration and hot press. (b) Photograph of the BN/PVA-D24 film. (c) Cross-sectional SEM images of BN/PVA-D24. ATR-FTIR deconvolution of (d) and (e) the –C–O(H) region, (f) the –NH_2 region, (g) the –C═O region and (h) the B–N region in BN/PVA-D24. (i) The HBD in different BN/PVA-D*X* composite films.

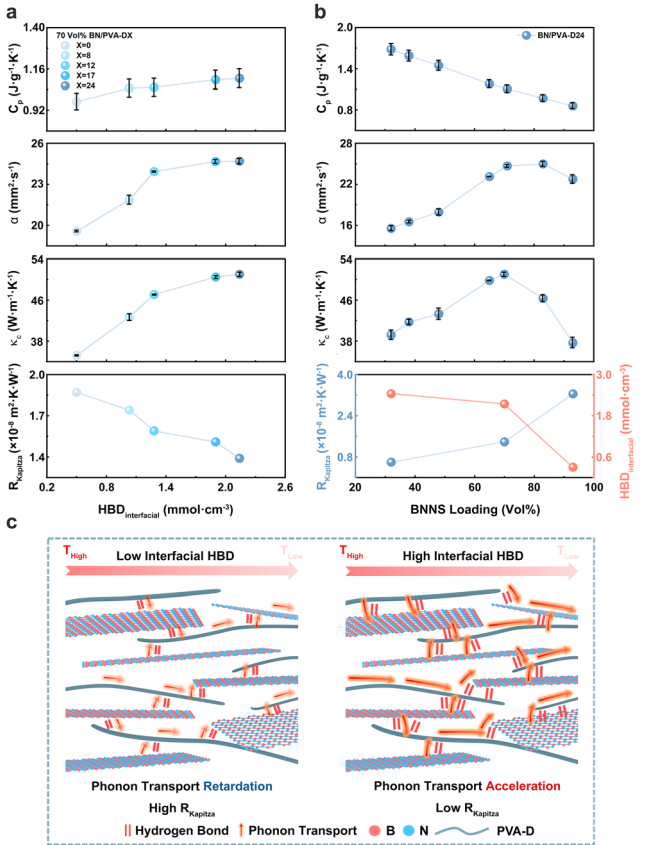

Fig. 5 Thermal Properties of BN/PVA-D*X* Composite Films. (a) Comparison of heat capacity (C_p), thermal diffusivity (α), thermal conductivity (κ_c), and $R_{Kapitza}$ of BN/PVA-D*X* with varying interfacial HBDs. (b) Comparison of C_p, α, κ_c, and $R_{Kapitza}$ of BN/PVA-D24 composite films with increasing BNNS contents. (c) Schematic diagram depicting phonon transport under low and high interfacial HBD.

juxtaposes literature data for composites with and without platelet alignment. Aligned systems may exhibit lower $R_{Kapitza}$ and higher filler efficiency ($\kappa_c/\varnothing_f$). In our work, filtration followed by hot-pressing preserves the high in-plane orientation of the platelets, giving an orientation factor $\cos^2\theta \approx 1$. The additional hydrogen bonds introduced by PVA-D*X* reduce $R_{Kapitza}$ from 1.87×10^{-8} to 1.39×10^{-8} m^2 K W^{-1}, delivering a further ~20% increase in $\kappa_c/\varnothing_f$ relative to the state-of-the-art benchmarks. These results confirm that the exceptional heat-transfer performance arises from the synergy between maintained platelet alignment and engineered hydrogen-bonded interfaces.

Non-equilibrium molecular dynamics (NEMD) simulations (details provided in the Session S6, ESI†), which calculate $R_{Kapitza}$ based on temperature variations across the matrix–filler interface, further corroborate this trend (Fig. S13h, ESI†). Note that, κ_c rises steeply with interfacial HBD up to ~2.14 mmol cm^{-3} and then plateaus, mirroring the trend of thermal diffusivity α. Although $R_{Kapitza}$ continues to decline beyond this point, κ_c no longer increases, implying that interfacial resistance is no longer the principal bottleneck. Instead, phonon scattering within individual BN platelets, limited platelet–platelet contact area, and the low intrinsic thermal conductivity of the PVA-D*X* matrix dominate heat transport. Thus, once interfacial bonding sites are effectively saturated, further gains require strategies that improve the bulk filler network, such as promoting platelet alignment, or employing a higher κ polymer matrix, rather than additional hydrogen bonding engineering.

Next, we explored the effect of BNNS content by incorporating BNNS fillers at various loadings into the PVA-D24 matrix (the highest-HBD system). As shown in Fig. 5(b), although increasing BNNS loading initially elevates α, an excessive filler fraction (93 vol%) reduces it—likely due to fewer effective interfacial hydrogen bonds. Consequently, the BN/PVA-D24 composite with 70 vol% BN attains the maximum κ_c of 51.01 W m^{-1} K^{-1}, whereas raising loading to 93 vol% decreases κ_c to 37.67 W m^{-1} K^{-1}. This reduction can be attributed to the elevated $R_{Kapitza}$ arising from the decline in interfacial HBD as BN concentration increases (Fig. 5(b), bottom). For instance, at a moderate filler fraction (32 vol%), the composite exhibits a high interfacial HBD of 2.44 mmol cm^{-3} and a correspondingly low $R_{Kapitza}$ of 0.60×10^{-8} m^2 K W^{-1}. In stark contrast, at the highest filler fraction (93 vol%), where the interfacial HBD drops to 0.3 mmol cm^{-3}, $R_{Kapitza}$ rises to 3.25×10^{-8} m^2 K W^{-1}—an increase of approximately 442% (Table S29, ESI†). This observation underscores the critical balance between filler loading and interfacial hydrogen bonding in governing the thermal transport performance of BN/PVA composites.

Overall, our findings demonstrate that increased HBD acts as molecular "bridges," significantly enhancing phonon transport by pulling polymer chains closer to the BNNS surface and reinforcing interfacial interactions (details provided in ESI,† Section S8). As schematically illustrated in Fig. 5(c), increasing interfacial HBD expands phonon conduction pathways while reducing scattering, thereby lowering $R_{Kapitza}$ and enhancing κ_c. By optimizing HBD in BN/PVA composites, we achieved a state-of-the-art filler effectiveness ($\kappa_c/\varnothing_f$), of up to 120 W m^{-1} K^{-1} (Fig. 1(b)).

Conclusions

In this study, we have demonstrated that engineering interfacial hydrogen bond density (HBD) is a pivotal strategy for enhancing the thermal conductivity of BNNS-reinforced PVA composites. By systematically grafting DOPA onto the PVA matrix, we successfully increased the HBD, which in turn significantly reduced the interfacial thermal resistance ($R_{Kapitza}$). The optimized BN/PVA-D24 composite achieved a remarkable thermal conductivity of 51.01 W m^{-1} K^{-1} at a 70 vol% BNNS loading, highlighting an extremely low $R_{Kapitza}$ of 0.60×10^{-8} m^2 K W^{-1} and a filler effectiveness of up to 120 W m^{-1} K^{-1}. This performance is attributed to the formation of robust hydrogen bond networks that facilitate efficient thermal transport across the filler–matrix interfaces, as evidenced by both experimental measurements and molecular dynamics simulations. Furthermore, our findings reveal a saturation effect at high HBD levels, emphasizing the necessity of balancing filler loading with interfacial bonding to maximize thermal performance. This work provides critical insights into the interplay between filler content, interfacial interactions, and thermal transport mechanisms, offering a scalable and effective pathway for the design of high-performance polymer composites. Future research may explore the extension of this hydrogen bond engineering approach to other polymer–filler systems, broadening the applicability of this strategy in various thermal management technologies.

Author contributions

Wenbo Lin: data curation, formal analysis, validation, methodology, investigation, writing – original draft preparation; Yanfeng Li: data curation, formal analysis, writing – review & editing; Xirui Liu: data curation, formal analysis, writing – review & editing; Rui Xu: data curation, formal analysis, writing – review & editing; Jiajing Huang: data curation, formal analysis, writing – review & editing; Zhiyuan Jiang: methodology, supervision, writing – review & editing; Zhiguo Qu: methodology, supervision, writing – review & editing; Kai Xi: conceptualization, methodology, supervision, funding acquisition, writing – review & editing; Yue Lin: conceptualization, formal analysis, methodology, investigation, supervision, funding acquisition, writing – review & editing.

Data availability

The data supporting this article have been included as part of the ESI.†

Conflicts of interest

There are no conflicts to declare.

Acknowledgements

We acknowledge support from the National Natural Science Foundation of China (52273029, 92472124, 52402305 and 22278329), Natural Science Foundation of Fujian Province for

Distinguished Young Scholars (2023J06045), the Self-deployment Project Research Program of Haixi Institutes, Chinese Academy of Science (CXZX-2023-JQ09), the high-level innovation and entrepreneurship talent project of Qinchuangyuan (No. OCYRCXM-2022-308), and the State Key Laboratory for Electrical Insulation and Power Equipment (no. EIPE23125).

References

1 Y. Wang, Z. Lu, A. K. Roy and X. Ruan, *J. Appl. Phys.*, 2016, **119**, 065103.
2 H. Zhan, Y. Nie, Y. Chen, J. M. Bell and Y. Gu, *Adv. Funct. Mater.*, 2020, **30**, 1903841.
3 C. Wong, S. Wang, L. Ren, J.-B. Xu, X. Zeng and R. Sun, *Adv. Funct. Mater.*, 2024, **34**, 2401157.
4 C. H. Lin, A. G. Izard, L. Valdevit and Y. Won, *Adv. Mater. Interfaces*, 2021, **8**, 2001423.
5 Z. Wang, Y. Zhang, J. Yi, N. Cai and J. Guo, *J. Alloys Compd.*, 2022, **928**, 167123.
6 D. Mao, J. Chen, L. Ren, K. Zhang, M. M. F. Yuen, X. Zeng, R. Sun, J.-B. Xu and C.-P. Wong, *Composites, Part A*, 2019, **123**, 260–269.
7 Y. Li, P. Liu, Y. Gao, Y. Feng, P. Li and X. Chen, *J. Energy Chem.*, 2024, **95**, 208–215.
8 C. Zhu, Z. Chen, R. Zhu, N. Sheng and Z. Rao, *Adv. Eng. Mater.*, 2021, **23**, 2100327.
9 N. Zhao, J. Li, W. Wang, W. Gao and H. Bai, *ACS Nano*, 2022, **16**, 18959–18967.
10 K. Wu, J. Wang, D. Liu, C. Lei, D. Liu, W. Lei and Q. Fu, *Adv. Mater.*, 2020, **32**, 1906939.
11 Q. Yan, F. E. Alam, J. Gao, W. Dai, X. Tan, L. Lv, J. Wang, H. Zhang, D. Chen, K. Nishimura, L. Wang, J. Yu, J. Lu, R. Sun, R. Xiang, S. Maruyama, H. Zhang, S. Wu, N. Jiang and C. T. Lin, *Adv. Funct. Mater.*, 2021, **31**, 2104062.
12 G. Gao, M. Sun, B. Dai, L. Yang, K. Liu, Z. Yang, J. Han and J. Zhu, *Macromol. Mater. Eng.*, 2022, **307**, 2200373.
13 X. Zhang, J. Li, Q. Gao, Z. Wang, N. Ye, J. Li and Y. Lu, *Adv. Funct. Mater.*, 2023, **33**, 2213274.
14 X. Shen, Z. Wang, Y. Wu, X. Liu and J.-K. Kim, *Carbon*, 2016, **108**, 412–422.
15 H. Bark, M. W. M. Tan, G. Thangavel and P. S. Lee, *Adv. Energy Mater.*, 2021, **11**, 2101387.
16 X. Jia, B. Liu, S. Li, X. Li, J. Zhou, G. Zhou, S. Wang, M. Xu, C. Xu, J. Du, Y. Deng and X. Huai, *J. Mater. Sci.*, 2022, **57**, 11026–11045.
17 Z. Xie, Z. Dou, D. Wu, X. Zeng, Y. Feng, Y. Tian, Q. Fu and K. Wu, *Adv. Funct. Mater.*, 2023, **33**, 2214071.
18 R. Landauer, *AIP Conf. Proc.*, 1978, **40**, 2–45.
19 A. G. Every, Y. Tzou, D. P. H. Hasselman and R. Raj, *Acta Metall. Mater.*, 1992, **40**, 123–129.
20 D. P. H. Hasselman and L. F. Johnson, *J. Compos. Mater.*, 1987, **21**, 508–515.
21 H.-B. Cho, T. Nakayama, H. Suematsu, T. Suzuki, W. Jiang, K. Niihara, E. Song, N. S. A. Eom, S. Kim and Y.-H. Choa, *Compos. Sci. Technol.*, 2016, **129**, 205–213.
22 G. Xin, H. Sun, T. Hu, H. R. Fard, X. Sun, N. Koratkar, T. Borca-Tasciuc and J. Lian, *Adv. Mater.*, 2014, **26**, 4521–4526.
23 X. Tong, L. Du and Q. Xu, *J. Mater. Chem. A*, 2018, **6**, 3091–3099.
24 J. Han, G. Du, W. Gao and H. Bai, *Adv. Funct. Mater.*, 2019, **29**, 1900412.
25 Y. Li, Y. Feng, M. Qin, K. Chen, Y. An, P. Liu, Y. Jiang, Z. Shen and X. Chen, *Small*, 2025, e2500479, DOI: **10.1002/smll.202500479**.
26 X. Chen, J. Lin, Y. Feng, K. Chen, M. Qin, S. Han, Y. Jiang, Z. Shen and Y. Li, *Carbon*, 2025, **238**, 120192, DOI: **10.1016/j.carbon.2025.120192**.
27 J. Huang, S. E, J. Li, F. Jia, Q. Ma, L. Hua and Z. Lu, *ACS Appl. Nano Mater.*, 2021, **4**, 13167–13175.
28 H. Yu, P. Guo, M. Qin, G. Han, L. Chen, Y. Feng and W. Feng, *Compos. Sci. Technol.*, 2022, **222**, 109406.
29 J. Chen, H. Wei, H. Bao, P. Jiang and X. Huang, *ACS Appl. Mater. Interfaces*, 2019, **11**, 31402–31410.
30 N. Jiang, Y.-Y. Song, L.-N. Wang, W.-W. Liu, L. Bai, J. Yang and W. Yang, *Adv. Funct. Mater.*, 2024, **35**, 2416277.
31 X. D. Zhang, G. Yang and B. Y. Cao, *Adv. Mater. Interfaces*, 2022, **9**, 2200078.
32 E. T. Swartz and R. O. Pohl, *Rev. Mod. Phys.*, 1989, **61**, 605–668.
33 G. Yang, X. Zhang, D. Pan, W. Zhang, Y. Shang, F. Su, Y. Ji, C. Liu and C. Shen, *ACS Appl. Mater. Interfaces*, 2021, **13**, 32286–32294.
34 H. He, W. Peng, J. Liu, X. Y. Chan, S. Liu, L. Lu and H. Le Ferrand, *Adv. Mater.*, 2022, **34**, 2205120.
35 Y. He, F. Kuang, Z. Che, F. Sun, K. Zheng, J. Zhang, X. Cao and Y. Ma, *Composites, Part A*, 2022, **157**, 106933.
36 C. Fu, Q. Li, J. Lu, S. Mateti, Q. Cai, X. Zeng, G. Du, R. Sun, Y. Chen, J. Xu and C.-P. Wong, *Compos. Sci. Technol.*, 2018, **165**, 322–330.
37 A. Rai and A. L. Moore, *Compos. Sci. Technol.*, 2017, **144**, 70–78.
38 J. Wang, P. Ren, Z. Chen, T. Wu, F. Wang and C. You, *Appl. Surf. Sci.*, 2023, **610**, 155309.
39 H. Zhang, Q. He, H. Yu, M. Qin, Y. Feng and W. Feng, *Adv. Funct. Mater.*, 2023, **33**, 2211985.
40 T. Huang, X. Zhang, T. Wang, H. Zhang, Y. Li, H. Bao, M. Chen and L. Wu, *Nano-Micro Lett.*, 2023, **15**, 2.
41 Q. Yan, W. Dai, J. Gao, X. Tan, L. Lv, J. Ying, X. Lu, J. Lu, Y. Yao, Q. Wei, R. Sun, J. Yu, N. Jiang, D. Chen, C.-P. Wong, R. Xiang, S. Maruyama and C.-T. Lin, *ACS Nano*, 2021, **15**, 6489–6498.
42 Y. Gao, M. Zhang, X. Chen, Y. Zhu, H. Wang, S. Yuan, F. Xu, Y. Cui, D. Bao, X. Shen, Y. Sun, J. Peng, Y. Zhou and M. Zhang, *Chem. Eng. J.*, 2021, **426**, 131280.
43 Z. Khan, F. Javed, Z. Shamair, A. Hafeez, T. Fazal, A. Aslam, W. B. Zimmerman and F. Rehman, *J. Ind. Eng. Chem.*, 2021, **103**, 80–101.
44 L. Chai, Q. Li, Y. Zhu, Z. Zhang, Q. Wang, Y. Wang and Z. Yang, *Bioresour. Technol.*, 2010, **101**, 6269–6272.
45 C. Korupalli, W.-Y. Pan, C.-Y. Yeh, P.-M. Chen, F.-L. Mi, H.-W. Tsai, Y. Chang, H.-J. Wei and H.-W. Sung, *Biomaterials*, 2019, **216**, 119268.
46 S. Hu, X. Pei, L. Duan, Z. Zhu, Y. Liu, J. Chen, T. Chen, P. Ji, Q. Wan and J. Wang, *Nat. Commun.*, 2021, **12**, 1689.
47 K. Gong, L. Hou and P. Wu, *Adv. Mater.*, 2022, **34**, 2201065.

48 L. Hou and P. Wu, *Carbohydr. Polym.*, 2019, **205**, 420–426.
49 J. Reignier, F. Méchin and A. Sarbu, *Polym. Test.*, 2021, **93**, 106972.
50 G.-H. Kim, D. Lee, A. Shanker, L. Shao, M. S. Kwon, D. Gidley, J. Kim and K. P. Pipe, *Nat. Mater.*, 2015, **14**, 295–300.
51 J. Chen, Z. Wang, B. Yao, Y. Geng, C. Wang, J. Xu, T. Chen, J. Jing and J. Fu, *Adv. Mater.*, 2024, **36**, 2401178.
52 J. Eichhorn, S. Schlögl, B. V. Lotsch, W. Schnick, W. M. Heckl and M. Lackinger, *CrystEngComm*, 2011, **13**, 5559–5565.
53 Y. Chen, Y. Liu, X. Liu, P. Li, Z. Li, P. Jiang and X. Huang, *Small Methods*, 2024, **8**, 2301386.
54 C.-W. Nan, X.-P. Li and R. Birringer, *J. Am. Ceram. Soc.*, 2004, **83**, 848–854.